REPORT DOCUMENTATION PAGE

Form Approved
OMB No. 0704-0188

1. REPORT DATE *(DD-MM-YYYY)*	2. REPORT TYPE	3. DATES COVERED *(From - To)*
20 Mar 2008	FINAL REPORT	1 Mar 2004 - 31 Jul 2007

4. TITLE AND SUBTITLE
QUANTUM LATTICE ALGORITHMS FOR 2D AND 3D MAGNETOHYDRODYNAMICS

5a. CONTRACT NUMBER
FA9550-04-1-0128

5b. GRANT NUMBER
03NM208

5c. PROGRAM ELEMENT NUMBER

6. AUTHOR(S)
Dr. Linda Vahala

5d. PROJECT NUMBER

5e. TASK NUMBER

5f. WORK UNIT NUMBER

7. PERFORMING ORGANIZATION NAME(S) AND ADDRESS(ES)
Dept of Electrical and Computer Engineering
OLD DOMINION UNIV RSH FOUNDATION INC.
Norfolk, VA 23508

8. PERFORMING ORGANIZATION REPORT NUMBER

9. SPONSORING/MONITORING AGENCY NAME(S) AND ADDRESS(ES)
AF OFFICE OF SCIENTIFIC RESEARCH
875 NORTH RANDOLPH STREET ROOM 3112
ARLINGTON VA 22203
Dr Jon Sjogren/NE

10. SPONSOR/MONITOR'S ACRONYM(S)

11. SPONSOR/MONITOR'S REPORT NUMBER(S)

12. DISTRIBUTION/AVAILABILITY STATEMENT
DISTRIBUTION STATEMENT A: UNLIMITED

AFRL-SR-AR-TR-08-0176

13. SUPPLEMENTARY NOTES

14. ABSTRACT
During the 3 years of this grant, we have continued our collaboration with Jeffrey Yepez (AFRL, Hancom Field) and George Vahala (William & Mary) on both quantum and entropic lattice algorithms for the solution of nonlinear physics problems. Because of the extreme scalability of the algorithms that we have been developing, we were chosen for CAP-Phase II for the new IBM-P5+ supercomputer (Babbage) at NAVO MSRC and also for CAP-Phase II on the 9000 core on the SGI-Altix at ASC.

15. SUBJECT TERMS
Nonlinear Physics; Quantum Lattice Algorithms; Entropic Lattice Algorithms

16. SECURITY CLASSIFICATION OF:			17. LIMITATION OF ABSTRACT	18. NUMBER OF PAGES	19a. NAME OF RESPONSIBLE PERSON
a. REPORT	b. ABSTRACT	c. THIS PAGE		14	19b. TELEPHONE NUMBER *(Include area code)*

AFOSR FINAL REPORT

"QUANTUM LATTICE ALGORITHMS FOR 2D AND 3D MAGNETOHYDRODYNAMICS"

November 2007

Linda Vahala
Old Dominion University

During the 3 years of this grant, we have continued our collaboration with Jeffrey Yepez (AFRL, Hancom Field) and George Vahala (William & Mary) on both quantum and entropic lattice algorithms for the solution of nonlinear physics problems. Because of the extreme scalability of the algorithms that we have been developing, we were chosen for CAP-Phase II for the new IBM-P5+ supercomputer (Babbage) at NAVO MSRC and also for CAP-Phase II on the 9000 core on the SGI-Altix at ASC.

What is very interesting is the analogy between the detailed balance quantum lattice algorithms and entropic lattice Boltzmann algorithms.

At each space-time grid point $(\mathbf{x},t)$ in lattice algorithms, the excited state of a qubit $|q\rangle$ encodes the probability f_q of the existence of a mesoparticle moving with discrete lattice velocity $\mathbf{c}_q = \Delta\mathbf{x}_q / \Delta t$. $\Delta\mathbf{x}_q$ are the lattice vector links, with $q = 1,2, \ldots. Q$, where Q is the number of qubits at each spatial node. The particle momentum is determined from a suitably chosen qubit-qubit interaction Hamiltonian H' while the spatial location arises from the free-streaming Hamiltonian $-i\hbar\sum_q \mathbf{c}_q \cdot \nabla$. All the particle-particle interactions generated by H' (from 2-body up to Q-body interactions) can be mapped onto a local collision operator $\Omega_q(f_1 \ldots . f_Q)$ at $\mathbf{x}$. In particular, for type-II quantum algorithms, the quantum entanglement is localized to those Q-qubits at $(\mathbf{x},t)$ and then this entanglement is spread throughout the lattice by unitary streaming[3,4]:

$$f_q'(\mathbf{x},t) = f_q(\mathbf{x},t) + \Omega_q(f_1 \ldots . f_Q) \ , \ f_q(\mathbf{x} + \Delta\mathbf{x}_q, t + \Delta t) = f_q'(\mathbf{x},t) \quad . \tag{1}$$

Here f_q is the incoming probability and f_q' the outgoing probability. In the classical limit, there exists a fundamental discrete entropy function[1,2,5]

$$\mathrm{H}(f_1 \ldots f_Q) = \sum_{q=1}^{Q} f_q \ln(f_q / w_q), \tag{2}$$

where the normalized weights $\left(\sum_q w_q = 1\right)$ are determined self-consistently. The collision operator Ω_q in Eq. (1) is determined so that one remains on a constant entropy surface

$$\mathrm{H}(f_1' \ldots . f_Q') = \mathrm{H}(f_1 \ldots f_Q) \quad . \tag{3}$$

Eqs. (1)-(3) constitute the basics of the detailed-balance lattice algorithms for fluid turbulence that are ideal for parallel (both classical and quantum) supercomputers.

In the Q-dimensional velocity space, the relaxation distribution function f_q^{eq} is determined analytically by extremizing the H-function subject to the local collisional constraints of conservation of probability and probability flux. f_q^{eq}, considered as a vector, is the bisector of the difference between the incoming and outgoing kinetic vectors in the inviscid limit $\lim_{\mu \to 0} \alpha / 2\tau = 2$:

$$f_q = f_q^{eq} - \frac{2\tau}{\alpha}\,\Omega_q \;\;,\;\; f_q^{'} = f_q^{eq} + \left(1 - \frac{2\tau}{\alpha}\right)\Omega_q \tag{4}$$

Eliminating Ω_q and $f_q^{'}$ from Eqs. (4) and (1) one obtains the lattice Boltzmann (LB) equation

$$f_q\left(\mathbf{x} + \Delta\mathbf{x}_q, t + \Delta t\right) = f_q\left(\mathbf{x},t\right) + \frac{\alpha}{2\tau}\left[f_q^{eq}\left(\mathbf{x},t\right) - f_q\left(\mathbf{x},t\right)\right] \;\;,\;\; q = 1....Q \tag{5}$$

This is basically the entropic LB[1,2] with the BGK collisional relaxation parameters $\alpha\left(\mathbf{x},t\right)/2\tau$ and f_q^{eq} determined from Eqs. (2) and (3). In the Chapman-Enksog limit, $\left(\Delta\mathbf{x} \to 0\;,\; \Delta t \to 0\right)$-- and identifying the density and momentum moments $\sum_q f_q = \rho$, $\sum_q \mathbf{c}_q f_q = \rho\,\mathbf{u}$ -- one recovers the quasi-incompressible Navier-Stokes equation with

$$\text{effective viscosity: } \mu\left(\mathbf{x},t\right) = \frac{1}{6}\left(\frac{4\tau}{\alpha\left(\mathbf{x},t\right)} - 1\right) \;;$$

$$\text{molecular viscosity: } \mu_0 = \frac{1}{6}\left(2\tau - 1\right) \;,\; \tau > 0.5 \tag{6}$$

To avoid discrete lattice geometry effects polluting the turbulence simulations, one is restricted to certain Q's on a cubic lattice. In particular it can be shown that on a unit cubic lattice, the lowest order kinetic velocity models are

Q15: rest velocity, speed 1 (6 velocities), speed $\sqrt{3}$ (8 velocities) – i.e., $Q = 15$

Q19: rest velocity, speed 1 (6 velocities), speed $\sqrt{2}$ (12 velocities) – i.e., $Q = 19$

Q27: rest velocity, speed 1 (6), speed $\sqrt{2}$ (12), and speed $\sqrt{3}$ (8) – i.e., $Q = 27$ (7)

Because detailed balance is in-built into the entropic LB algorithm [see Eq. (3)], the scheme is unconditionally stable for arbitrary large Reynolds numbers, $\mathrm{Re} = U_0 L / 2\pi\mu_0$.

In the CAP-II runs on 9000 cores on Hawk, we concentrated on the Lattice Boltzman MHD code. In particular we have been considering the lattice Boltzmann simulation for the initial profiles of a Taylor-Green velocity profile in an Orszag-Tang magnetic field:

$$\mathbf{u}(\mathbf{x},\, t=0) = U_0\,\left(\sin x \cos y \cos z\;,\; -\cos x \sin y \cos z,\; 0\right)$$

$$\mathbf{B}(\mathbf{x},\, t=0) = B_0\,\left(-2\sin 2y + \sin z,\; 2\sin x + \sin z,\; \sin x + \sin y\right)$$

The isosurfaces of vorticity and current shown in Fig. 1

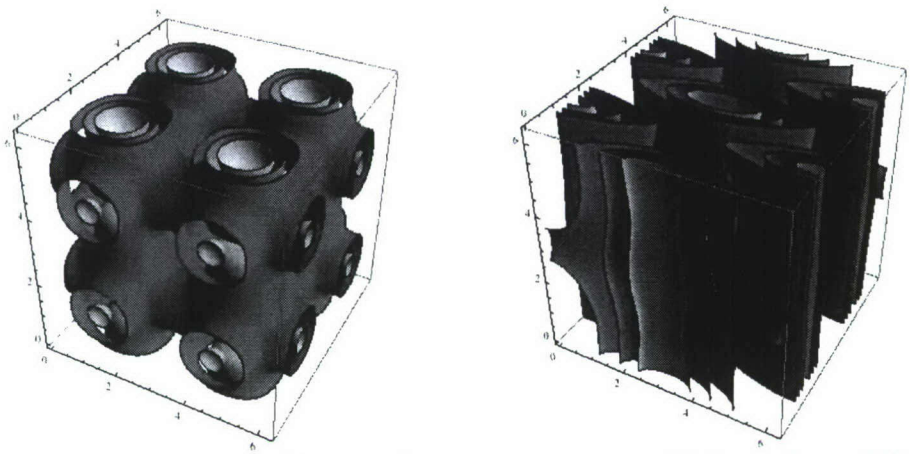

Fig.1 (a) Isosurfaces of |Vorticity| *(b) Isosurfaces of |Current|*

With these profiles, there is no initial magnetic helicity or cross helicity

$$0 = \int d^3x\, \mathbf{A}(\mathbf{x},0)\cdot\mathbf{B}(\mathbf{x},0) \quad , \quad 0 = \int d^3x\, \mathbf{u}(\mathbf{x},0)\cdot\mathbf{B}(\mathbf{x},0)$$

where **A** is the vector potential.

An extremely important property of the LB algorithm for MHD is that from the Chapman-Enksog expansions one can show that the trace of the first order magnetic stress tensor is proportional the divergence of the magnetic field – and hence this must be zero since the magnetic stress tensor is antisymmetric:

$$0 = Tr\Lambda^{(1)} = \sum_{\alpha,\, i} e_{\alpha i}\left[g_{\alpha i} - g^{eq}_{\alpha i} \right] = -\frac{\tau_B}{3}\nabla\cdot\mathbf{B}$$

We have verified this result directly from our LB simulations by explicitly calculating the trace of the magnetic stress tensor, Fig. 2, with $Tr\Lambda^{(1)} = 0$ to machine accuracy.

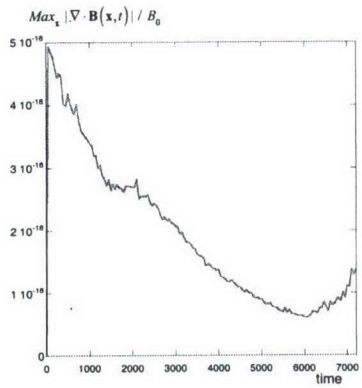

Fig.2 The time evolution of $Tr\Lambda^{(1)}(t) = \sum_{\alpha,\, i} e_{\alpha i}\left(g_{\alpha i} - g^{eq}_{\alpha i}\right)$ *in the LB simulation, showing it is 0 to machine accuracy. Chapman-Enskog asymptotics yields* $Tr\Lambda^{(1)} = -\tau_B\nabla\cdot\mathbf{B}/3$.

We present results from two large simulation runs on a spatial lattice of $1800\times1800\times1800$ using all the 9000 cores available on the SGI Altix. The first run ran for 60 K time steps with

$$CASE\ A:\ \mathrm{Re} = \frac{U_0 L}{\nu} = 1000 \quad , \quad Rm = \frac{B_0 L}{\eta} = 350 \quad , \quad \mathrm{Pr} = \frac{\nu}{\eta} = 0.3 \quad ,$$

while the second run ran to 30K time steps at a higher Prandtl and magnetic Reynolds number

$$CASE\ B:\ \mathrm{Re} = \frac{U_0 L}{\nu} = 350\ ,\quad Rm = \frac{B_0 L}{\eta} = 1050\ ,\quad \mathrm{Pr} = \frac{\nu}{\eta} = 3.0$$

In Fig. 3 we plot the time development of the normalized energies, enstrophies and palinstrophy

$$E_{kin}(t) = \int d^3x\ \mathbf{u}^2(\mathbf{x},t)\ ,\quad E_{mag}(t) = \int d^3x\ \mathbf{B}^2(\mathbf{x},t)$$

$$Kinetic\ Enstrophy\ \Omega(t) = \int d^3x\ \left|\nabla \times \mathbf{u}(\mathbf{x},t)\right|^2 = \left\langle \boldsymbol{\omega}^2(\mathbf{x},t)\right\rangle$$

$$Magnetic\ Enstrophy\ \Omega_M(t) = \int d^3x\ \left|\nabla \times \mathbf{B}(\mathbf{x},t)\right|^2 = \left\langle \mathbf{J}^2(\mathbf{x},t)\right\rangle$$

$$Palinstrophy\ P(t) = \int d^3x\ \left|\nabla \times \boldsymbol{\omega}(\mathbf{x},t)\right|^2 = \left\langle \left|\nabla \times \boldsymbol{\omega}(\mathbf{x},t)\right|^2\right\rangle$$

which are just higher order $k-$ moments of the energy spectra.

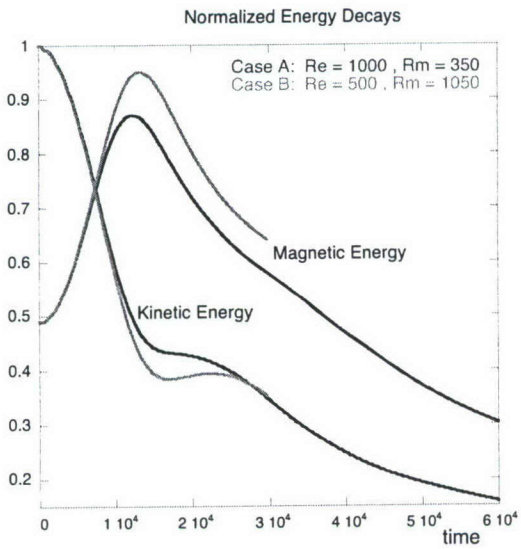

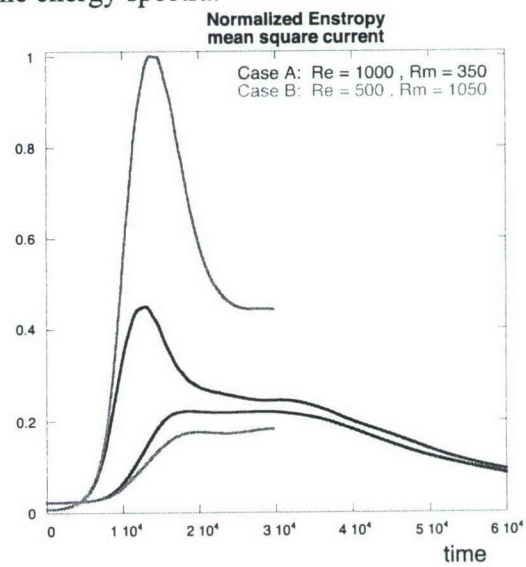

(a) normalized kinetic and magnetic energy *(b) normalized kinetic and magnetic enstrophy*

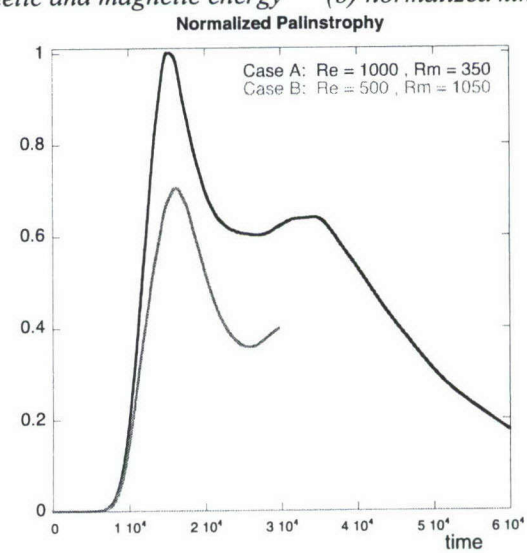

(c) normalized palinstrophy

Fig. 3 The time development of the (a) kinetic and magnetic energies, (b) the kinetic and magnetic enstrophy, and (c) the kinetic palinstrophy – normalized to peak value.

In Navier-Stokes turbulence, the kinetic enstrophy increases sharply at early times due to inviscid vortex stretching – i.e., the kinetic enstrophy increase is independent of the transport coefficient. The kinetic energy during this period is very slowly decreasing. In MHD, however, we see an immediate strong energy exchange from kinetic to magnetic which is independent of transport coefficients (Case A and B curves overlay in Fig. 4a for t < 10 K) with a rapid rise in the magnetic enstrophy (i.e., mean square current). For 10K < t < 20K, there is a flattening in the kinetic energy decay (Fig. 4a) and a subsequent increase in the kinetic enstrophy (Fig. 4b), somewhat akin to Navier-Stokes turbulence. The strength of the respective transport coefficient dictates which particular enstrophy peaks at a greater value (i.e., for Case B the lower resistivity and higher viscosity dictate that the magnetic enstrophy has a greater increase than in Case A while the kinetic enstrophy has a lower increase than in Case A). This is also seen in the sharp rise of the kinetic palinstrophy, Fig. 4c.

The directional energy spectra are shown in Fig. 5 (low magnetic Prandtl number, $\mathrm{Pr} = \nu / \eta = 0.3$) and Fig.6 (high magnetic Prandtl number, $\mathrm{Pr} = \nu / \eta = 3.0$). Initially these spectra are delta functions. The directional kinetic and magnetic spectra are defined by

$$E_{Kx}(k_x,t) = \sum_{k_y,\,k_z} \left|u_x(k_x,k_y,k_z,t)\right|^2 \quad , \quad E_{Ky}(k_x,t) = \sum_{k_y,\,k_z} \left|u_y(k_x,k_y,k_z,t)\right|^2$$

$$E_{Mx}(k_x,t) = \sum_{k_y,\,k_z} \left|B_x(k_x,k_y,k_z,t)\right|^2 \quad , \quad E_{My}(k_x,t) = \sum_{k_y,\,k_z} \left|B_y(k_x,k_y,k_z,t)\right|^2$$

where the summation is always over the wavenumbers k_y , k_z : the longitudinal spectra involve the x-component of the fields while the transverse spectra the y-component of the fields. In Fig. 4a, we plot the longitudinal [initially a $\delta(k_x - 2)$- spectrum] and the transverse [initially a two-delta function peak spectrum at $k_x = 2,\, 4$] directional kinetic energy at time = 30K, while in Fig. 4b the directional longitudinal magnetic energy spectrum at t = 10K, 20K, and 30K – and the comparison to the $k^{-5/3}$ Kolmogorov spectrum.

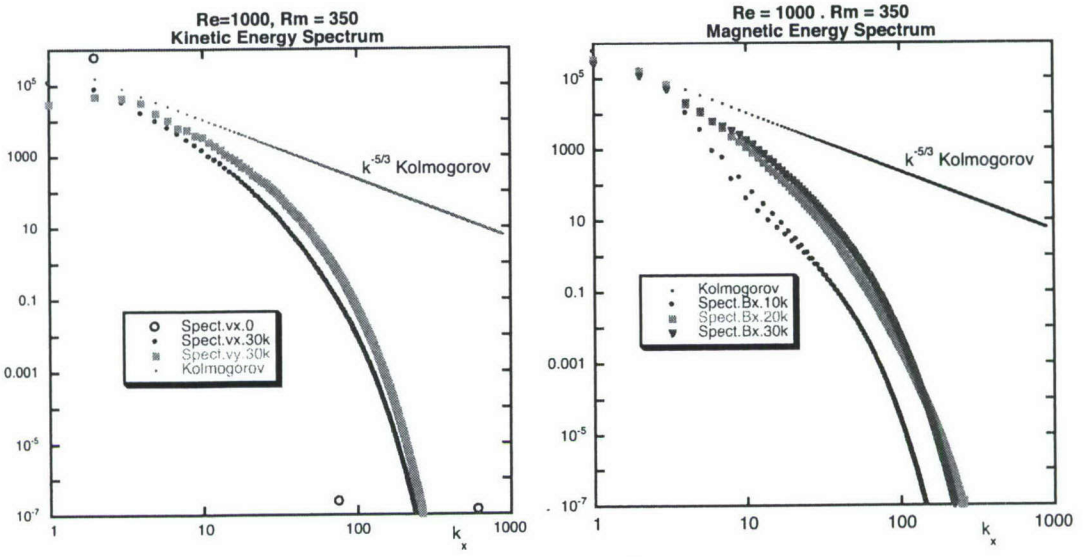

(a) *(b)*

Fig. 4 The time development of the directional energy spectra for the low magnetic Prandtl number case: $\mathrm{Pr} = \nu / \eta = 0.3$ *(a) the longitudinal and transverse kinetic energy spectrum at t = 30K, and (b) the longitudinal magnetic energy spectrum at t = 10K, 20K and 30K. Also plotted is the Kolmogorov* $k^{-5/3}$ *inertial range spectrum.*

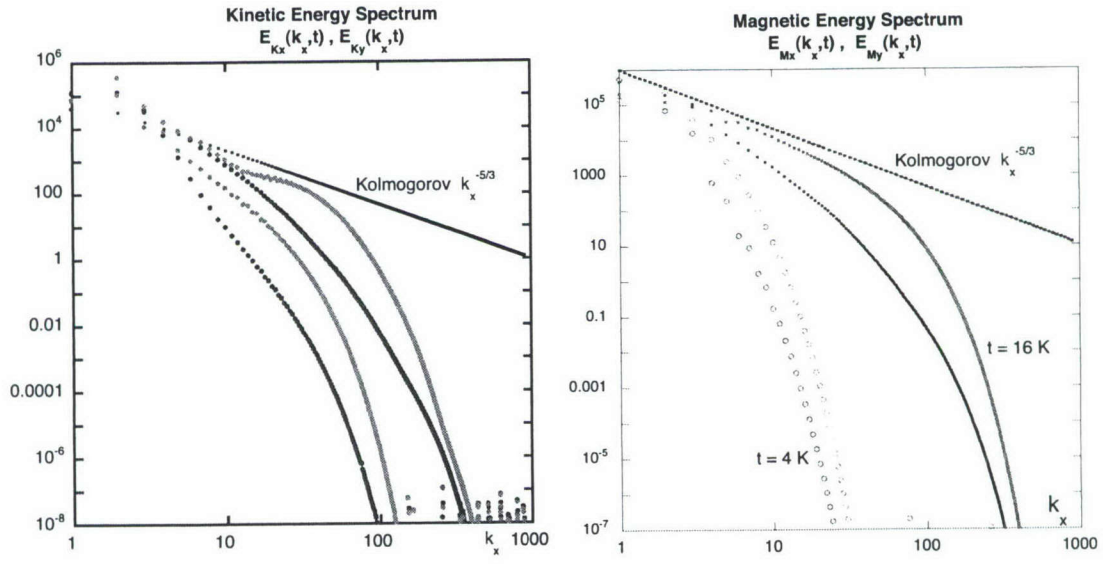

(a) *(b)*

Fig. 5 The time development of the directional energy spectra for the high magnetic Prandl number case: $\mathrm{Pr} = \nu / \eta = 3.0$ *(a) the longitudinal and transverse kinetic energy spectrum at t = 4K and t = 16K, and (b) the longitudinal and transverse magnetic kinetic energy spectrum at t = 4K and t = 16K. Also plotted is the Kolmogorov* $k^{-5/3}$ *inertial range spectrum.*

As we increase the magnetic Prandtl number to Case B one finds a substantial difference between the longitudinal and transverse spectra, Fig. 5. The transverse kinetic and magnetic energy spectra show much stronger excitation of high k_x-modes, which in the magnetic energy case shows a quite strong semblance to the Kolmogorov inertial energy

$k_x^{-5/3}$ - spectrum at t = 16K (Fig. 5b). There is also an interesting enhancement of the transverse kinetic energy spectrum for $40 < k_x < 200$ at t = 16K (Fig. 5a).

This behavior maybe attributed to the strong but localizd vorticity and current sheets developing due to the turbulence. In Fig. 6 we plot some time snapshots of the isosurfaces of vorticity and current for this high magnetic Prandtl number case.

vorticity isosurface

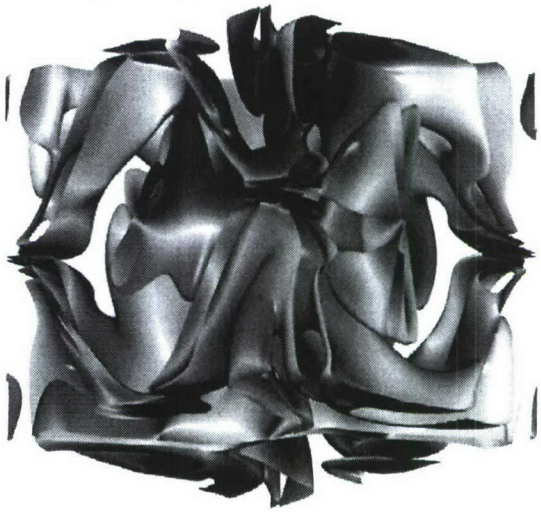

vorticity isosurface

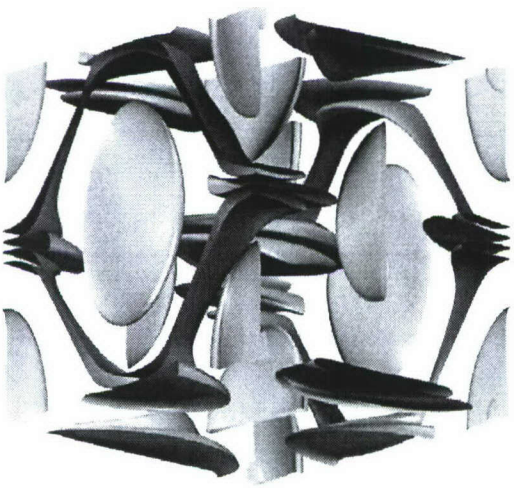

current isosurface

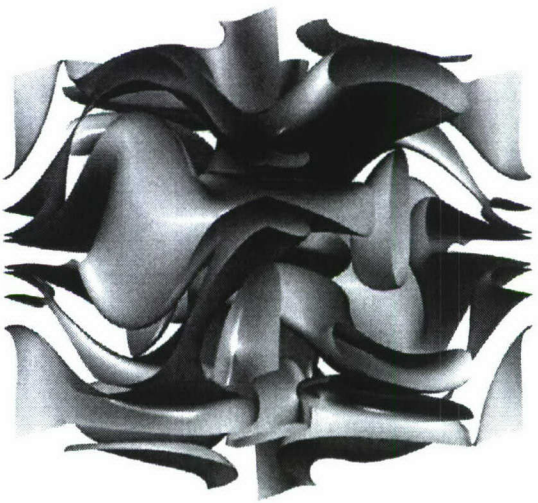

current isosurface

(a) t = 4K

(b) t = 8K

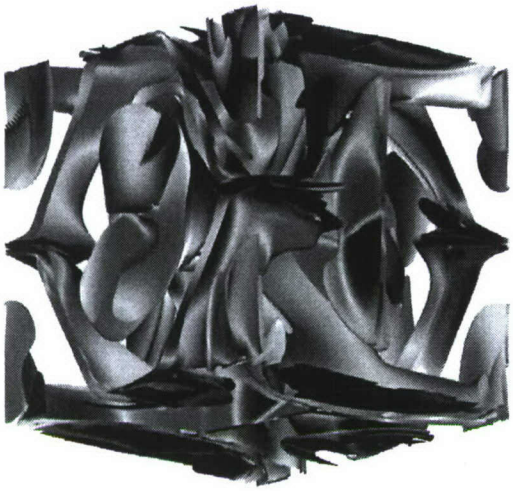

vorticity isosurface

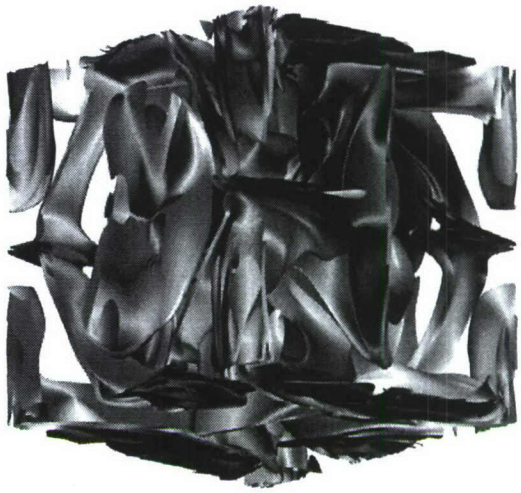

vorticity isosurface

current isosurface

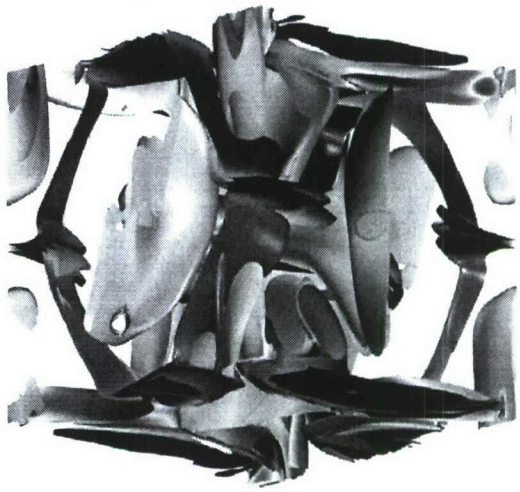

current isosurface

(c) t = 12K

(d) t = 16K

vorticity isosurface

vorticity isosurface

current isosurface

(e) t = 20K

current isosurface

(f) t = 24K

Fig. 6 The time development of the vorticty, $|\boldsymbol{\omega}|$, and corresponding current $|\mathbf{J}|$, isosurface for the high magnetic Prandtl number simulation. (a) t = 4K, (b) t = 8K, (c) t = 12K, (d) t = 16K, (e) t = 20K, (f) t = 24K. The isosurface value chosen is that corresponding to the average $|\boldsymbol{\omega}|$ and average $|\mathbf{J}|$ for that time instant. The color coding is dependent on the value of $\hat{\mathbf{u}}\cdot\hat{\boldsymbol{\omega}}$ and $\hat{\mathbf{B}}\cdot\hat{\mathbf{J}}$ at the isosurface gridpoint, going from RED for parallel unit vectors $\hat{\mathbf{u}} \| \hat{\boldsymbol{\omega}}$ to BLUE for antiparallel unit vectors $\hat{\mathbf{u}}\cdot\hat{\boldsymbol{\omega}} = -1$. Similarly for the current isosurfaces: from RED for $\hat{\mathbf{B}}\cdot\hat{\mathbf{J}} = +1$ to BLUE for $\hat{\mathbf{B}}\cdot\hat{\mathbf{J}} = -1$. The GREY scale is for isosurfaces with $\hat{\mathbf{u}}\cdot\hat{\boldsymbol{\omega}} = 0 = \hat{\mathbf{B}}\cdot\hat{\mathbf{J}}$

There is much information in Fig. 6 : the intensification of localized horizontal current sheets (see Fig. 6a-Fig.6c, midway at the vertical cube edges), the development of intense vertical localized patches of vorticity and current at later times with similar isosurface

geometrical structures of vorticity and current. It is also very apparent that large scale magnetic (and hence velocity) structures persist for long times, Fig.6f. This is also seen in the low magnetic Prandtl number simulation, Fig. 7, where some large scale vorticity and current isosurface structures persist, even at t = 50K. This is very unlike 3D Navier-Stokes turbulence which is dominated by small scale vortex structures as seen in Fig. 8

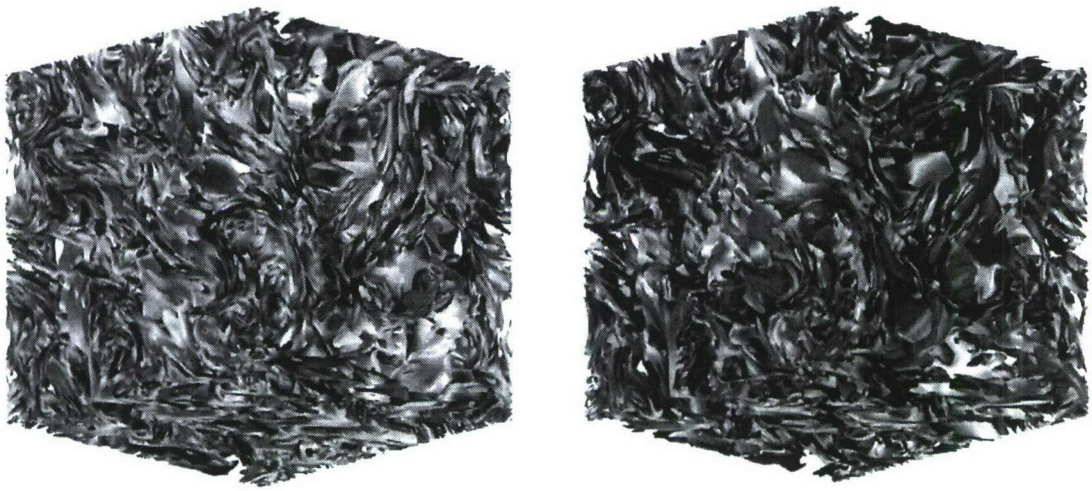

(a) (b)

Fig. 7 The (a) vorticity and (b) current isosurfaces at t = 50K for the low Prandtl number ($\mathrm{Pr} = \nu / \eta = 0.3$) *simulation. Some large scale magnetic structures persist, along with corresponding large scale vortex structures.*

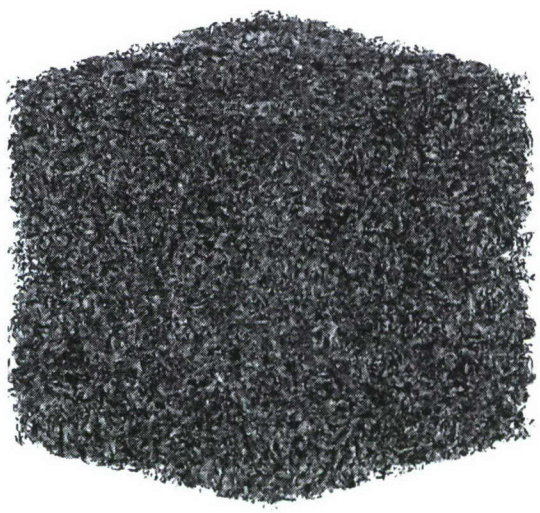

Fig. 8 The vorticity isosurfaces in 3D Navier-Stokes turbulence. The flow is dominated by very small scale structures after the inviscid vortex stretching and the peak in the fluid enstrophy. This isosurface is at t = 7K of an ELB simulation

Finally, we present some correlation data for the magnetic field

$$C_{long}(r) = \left\langle B_x(x,y,z)\ B_x(x+r,y,z) \right\rangle$$

$$C^{y}_{trans}(r) = \left\langle B_y(x,y,z)\, B_y(x+r,y,z) \right\rangle \quad , \quad C^{z}_{trans}(r) = \left\langle B_z(x,y,z)\, B_z(x+r,y,z) \right\rangle$$

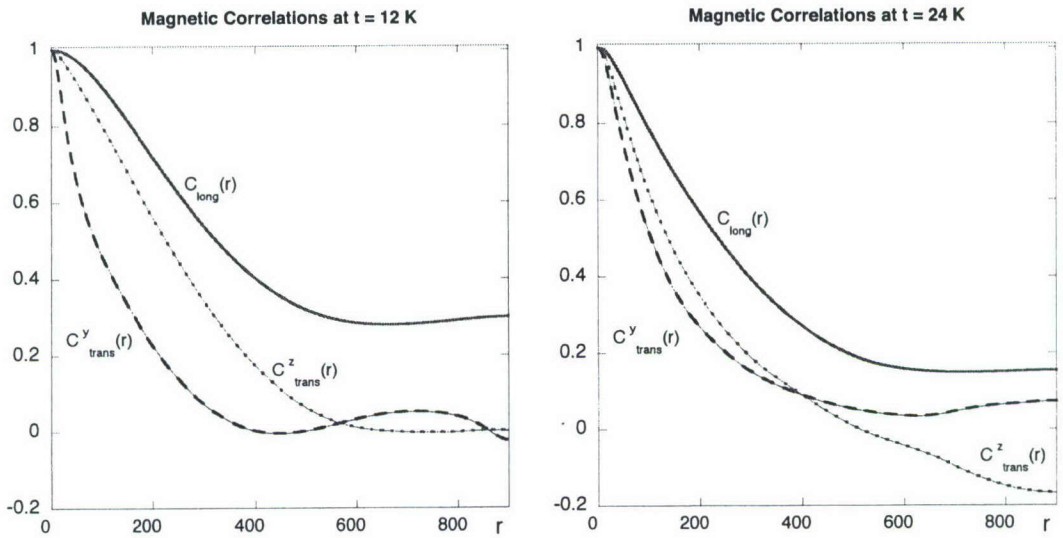

Fig. 14 Magnetic Correlations at (a) t = 12K, (b) t = 24K for the high magnetic Prandtl number simulation, Case B. The very slight increase in the longitudinal correlation function for r > 650 at t = 12K is no longer present at t = 24K.

It is seen that as time develops, the almost constant asymptotic tail of the longitudinal magnetic correlation function disappears, and by t = 28K $C_{long}'(r) < 0$ for all r. Moreover, we find (for $r > 0$)

$$C^{y}_{trans}(r) \ , \ C^{z}_{trans}(r) < C_{long}(r) \ , \text{ for all times}$$

with $C_{long}'(r) < 0$, are consistent with the correlation statistics of a random solenoidal vector field .

Concluding Remarks

We have developed a 3D LB-MHD algorithm that is ideally parallelized and presented some simulation results on a 1800^3-spatial grid that shows the persistence of large scale magnetic and vorticity structures for long times. Morever, the time development of the correlation statistics of the magnetic field indicate that the **B**-field is becoming more and more random. An important feature of the LB-MHD approach is that the algorithm automatically ensures $\nabla \bullet \mathbf{B} = 0$ to machine accuracy.

The straightforward LB algorithm, while simple and explicit, suffers from numerical instabilities as $\mathrm{Re} \to \infty$, $Rm \to \infty$. This places upper bounds on the attainable transport coefficients. At the Navier-Stokes level, entropic algorithms have been developed that remain unconditionally stable for arbitrary small viscosities. Indeed, we have presented here the first large scale ELB simulations on a 1600^3-grid at Re = 25000. While our ELB code runs successfully for much higher Reynolds numbers, the turbulence is no longer fully resolved on these 'small' grids, and so these results are not presented here. We are currently developing entropic LB-MHD algorithms that would permit simulations at arbitrary small transport coefficients.

While the simulations reported here are on a simple 3D periodic domain, LB algorithms can handle arbitrary geometries without loosing their intrinsic parallelization. Nonuniform spatial grids can be readily handled. In these cases, the spatial grid and the kinetic velocity lattice will now no longer overlay. As a result, the streaming step of the LB algorithm will no longer give immediate data at the spatial nodes. One would then resort to interpolation methods to get the streamed information onto the spatial nodes. Moreover all the latest CFD methods for handling arbitrary spatial grid geometries can be immediately brought over to LB. It remains to be seen what price will need to be paid on the parallelization of such augmented LB codes.

Finally, we comment on another interesting aspect of ELB algorithms. The ELB-viscosity $\nu_{eff}(\mathbf{x},t)$ gives the appearance of an eddy viscosity and immediately raises the question of whether there is any connection between ELB and the Large Eddy Simulations (LES) in turbulence modeling. The simplest LES model is the Smagorinsky model in which the subgrid scales are modeled by an eddy viscosity that is related to the mean rate of strain velocity tensor:

$$\nu_{smag}(\mathbf{x},t) = (C_s\Delta)^2 \sqrt{S_{ij}S_{ij}}$$

where the rate of strain tensor (of the resolvable scales)

$$S_{ij} = \frac{1}{2}\left(\frac{\partial u_i}{\partial x_j} + \frac{\partial u_j}{\partial x_i}\right)$$

Δ is the filter width (defined in the filtering function that separates the resolvable from the subgrid scales) and C_S is some empirical constant. Obviously, the connection (if any) between the ELB and LES transport coefficients is not obvious: ELB deals with entropy surfaces and the determination of the collision parameter $\gamma(\mathbf{x},t)$ that enforces detailed balance on the pre- and post-collision distribution functions, while LES deals with the rate of strain tensor. It is of much interest that one can immediately construct local LB-LES models that recover the Smagorinsky-CFD LES model. This is because the local strain tensor can be recovered from the second moment of the non-equilibrium distribution function

$$S_{ij} = \frac{1}{2}\left(\frac{\partial u_i}{\partial x_j} + \frac{\partial u_j}{\partial x_i}\right) = -\frac{3}{2\rho\,\tau_u}\sum_{\alpha} e_{\alpha i}e_{\alpha j}\left[f_\alpha - f_\alpha^{eq}\right]$$

Of course, this is exactly how $\nabla\bullet\mathbf{B}$ is recovered from the trace of the *first* moment of the nonequilibrium magnetic distribution function and by making this first moment antisymmetric we enforce $\nabla\bullet\mathbf{B} = 0$ to better than $O\left(10^{-15}\right)$. This also opens up the possibility of examining LES LB-MHD algorithms being developed for CFD techniques by Carati et. al., where the LB version will be, unlike the CFD code, ideally parallelized. These LES LB-MHD codes are currently being developed.

Publications During this Grant Proposal

"MHD Turbulence Studies using Lattice Boltzmann Algorithms"
G.Vahala, B. Keating, M. Soe, J. Yepez, L. Vahala, J. Carter and S. Ziegeler
Commun. in Computat. Phys. (accepted for publication, to appear 2008)

"Entropic Lattice Boltzmann Representations Required to Recover Navier-Stokes Flows"
B. Keating, G. Vahala, J. Yepez, M. Soe and L. Vahala
Physical Review **E75**, 036712 [1-11] (2007)

"Lattice Model of Fluid Turbulence"
J. Yepez, G. Vahala, L. Vahala, M. Soe and S. Ziegeler
Navigator NAVO MSRC , Spring 2007, pp. 12-19

"Lattice Boltzmann Algorithms for Fluid Turbulence"
G. Vahala, J. Yepez, M. Soe, L. Vahala and S. Ziegeler
in *HPCMP User Group Conference 2007*, pp. 52-56, *IEEE Computer Society*

"Quantum Lattice Representations for Vector Solitons in External Potentials"
G. Vahala, L. Vahala and J. Yepez
Physica **A362**, 215-221 (2006)

"Performance of Lattice Boltzmann Codes for NAvier-Stokes and MHD Turbulence on the Major Computer Architectures"
G. Vahala, J. Carter, M. Soe, J. Yepez, L. Vahala and A. Macnab
Parallel CFD 2005 (Elseiver Press, 2006)

"Lattice Quantum Algorithm for the Schrodinger Wave Equation in 2+1 Dimensions with a Demonstration by Modeling Soliton Instabilities"
J. Yepez, G. Vahala and L. Vahala
Quantum Info. Process. **4**, 457- 469 (Dec. 2005)

"Quantum Lattice Representation of 1D MHD turbulence with arbitrary Transport Coefficients"
J. Yepez, G. Vahala and L. Vahala
SPIE Conf. Proc. **5815**, 227-235 (2005)

"Magnetohydrodynamic Turbulence Simulations on the Earth Simulator Using the Lattice Boltzmann Method"
J. Carter, M. Soe, L. Oliker, Y. Tsuda, G. Vahala, L. Vahala and A. Macnab
International Conf. on High Computing, SC|05 (Nov. 2005, Seattle), Gordon-Bell Finalist Paper ISBN #1-59593-061-2

"Inelastic Vector Soliton Collisions: A Quantum Lattice Gas Representation"
G. Vahala, L. Vahala and J. Yepez
Phil. Trans.. Roy Soc. London **362**, 1677 – 1690 (2004)

"Quantum lattice gas representation of dark solitons"
G. Vahala, L. Vahala, and J. Yepez
SPIE Conf. Proc. **5436**, 376 – 385 (2004)